Proceedings of the Combustion Institute 42 (2026) 106281

Contents lists available at ScienceDirect

Proceedings of the Combustion Institute

journal homepage: www.elsevier.com/locate/proci

Ammonia combustion in a radial-inflow porous media burner: Effects of varied topological gradation

Guguloth Mahesh Nayak *, Max Bernard, Vladimir Erenburg, Beni Cukurel, Joseph K. Lefkowitz

The Stephen B. Klein Faculty of Aerospace Engineering, Technion - Israel Institute of Technology, Haifa, 320003, Israel

ARTICLE INFO

Keywords:
Porous media combustion
Silicon carbide porous inert media
Zero-carbon combustion
Micro gas turbine
High energy density burner
Ammonia combustor

ABSTRACT

This study investigates ammonia (NH_3) and ammonia–hydrogen (NH_3/H_2) combustion in a radial inward-flow porous media burner using silicon carbide (SiC) porous inert media (PIM) with systematically varied topology. Five PIM configurations were examined: two uniform structures, two graded structures with pore diameter and porosity increasing from the outer to the inner radius, and one reverse-graded structure. This topology matrix enables direct assessment of how pore architecture governs flame stabilization, gas–solid heat recirculation, and pollutant formation. Two mixture compositions were considered, pure NH_3 and 30 vol.% H_2 enrichment. For pure NH_3 operation, the graded structures exhibited the widest stability range, resulting in stable operation for $0.8 \leq \phi \leq 1.3$, whereas the uniform structures were stable only over $0.9 \leq \phi \leq 1.1$. With 30 vol.% H_2 enrichment, the operability broadened to $0.5 \leq \phi \leq 1.5$ across all tested topologies. Solid-phase temperatures were measured using spectrally filtered infrared imaging in a wavelength band that isolates SiC surface emission from gas-phase emission. The temperature fields revealed two stabilization regimes: dynamic stabilization in the inward-graded structures, where the flame location shifts with equivalence ratio, and fixed stabilization in the uniform and reverse-graded structures. Among the tested configurations, the inward-graded structure with finer pores produced the highest peak solid temperature, indicating the strongest heat recirculation and the most favorable conditions for ammonia conversion. Exhaust-gas analysis showed that lean operation suppresses NO formation while promoting N_2O emissions, whereas unburned NH_3 and H_2 slip become significant under rich conditions. The emissions hierarchy was found to depend strongly on flame stabilization location and the associated thermal coupling within the porous matrix. Overall, the results identify pore-topology effects that govern the trade-off between flame stability, combustion completeness, and NO/N_2O emissions in compact ammonia-fueled porous burners.

Novelty and significance statement: This work extends the understanding of radial inward-flow porous media burners for ammonia and ammonia–hydrogen combustion by systematically examining how varied porous topology governs flame stabilization, heat recirculation, and pollutant formation. Five silicon carbide Voronoi porous structures, including uniform, inward-graded, and reverse-graded configurations, are used to isolate the effects of pore size, porosity distribution, and gradient direction on burner performance. The measurements reveal two distinct stabilization regimes, dynamic and fixed, and establish how the local porous architecture controls the flame location and the associated emissions behavior. In addition, spectrally filtered infrared imaging is applied to isolate solid-phase emission from gas-phase emission, enabling spatially resolved characterization of the porous matrix temperature during ammonia combustion. These results provide physically grounded design guidelines for compact porous burners targeting stable and low-emission ammonia-based combustion systems.

1. Introduction

Porous media burners (PMBs) have long been recognized for their ability to intensify gas–solid heat exchange within the porous matrix, thereby enhancing heat recirculation, flame stabilization, and thermal efficiency [1–4]. In such systems, the porous structure does not merely support combustion mechanically, but actively governs the thermal environment through coupled conduction, convection, and radiation. As

* Corresponding author.
E-mail address: gmaheshnayak@campus.technion.ac.il (G.M. Nayak).

https://doi.org/10.1016/j.proci.2026.106281
Received 15 March 2026; Accepted 8 June 2026

a result, PMB performance is strongly dependent on porous topology, including pore diameter, porosity, and their spatial distribution, which together determine the local transport characteristics and the flame anchoring behavior.

Conventional PMBs often employ a two-zone concept, in which the flame stabilizes near the interface between porous regions of different thermal and hydraulic properties [5]. More recently, spatially graded porous matrices have been shown to provide an alternative stabilization mechanism, in which continuous variation of radiative extinction and interphase heat exchange allows the flame to shift within the structure and adapt to operating conditions [6,7]. Step-graded porous media have likewise been reported to extend lean operability while reducing pollutant emissions and improving thermal-shock tolerance [8, 9]. While most studies have relied on stochastic open-cell ceramic foams, triply-periodic minimal surface (TPMS) based architectures have recently emerged as an alternative, offering extended flammability and enabling optically accessible flame front tracking [10–12]. These features are especially attractive for ammonia (NH_3) combustion, for which flame stabilization remains challenging due to low reactivity and poor burning characteristics [13,14]. Although hydrogen enrichment improves flame speed and combustion stability, it can also increase NO_x formation in conventional burners [15,16]. PMBs are therefore of particular interest for ammonia-fueled systems, because their internal heat recirculation can compensate for the low reactivity of NH_3, while moderating peak temperatures relative to free-flame combustion, offering potential reduction in emissions.

Ammonia combustion in PMBs has received increasing attention in recent years, as summarized in the review by Makaryan et al. [17]. Among the available studies, the experimental investigations of Vignat and co-workers [18–20] provide the most comprehensive picture of NH_3/H_2 combustion in axial porous burners. Their work showed, in particular, that the use of multilayer silicon carbide (SiC) foams with larger pore sizes near the interface can improve ammonia-flame stabilization [19]. In parallel, reduced-order chemical reactor network modeling has been developed to interpret pollutant formation in such systems, while also highlighting the limitations for predicting stability limits. Subsequent improvements in volume-averaged modeling have incorporated detailed structural characterization of the porous matrix using X-ray computed microtomography [21], reflecting the growing recognition that porous topology plays a central role in determining NH_3/H_2 combustion behavior [22].

Recent ammonia-PMB studies have also increasingly explored staged configurations as a route toward lower emissions [20,23,24]. Rich–lean staging has been shown to reduce both NO emissions and unburned NH_3 relative to single-stage PMBs [20]. However, the performance of two-stage burners remains highly sensitive to the placement of the secondary-air injection and to the air ratio, with excessive secondary-air fractions (>25%) leading to incomplete combustion [24]. Moreover, extending the number of ceramic-foam layers, while beneficial for emissions control, introduces penalties in pressure drop, power density, and overall compactness. These limitations are important for applications in which space, mass, and aerodynamic integration are constrained.

In this context, compact radial porous burner configurations offer a distinct alternative to conventional axial multilayer designs. Our previous study demonstrated that a radially inward-flow PMB can sustain pure NH_3 combustion over a broad range of equivalence ratios and mass fluxes, while achieving low NO emissions near lean-extinction conditions for NH_3/H_2 mixtures [25]. Such a high-power-density burner architecture is particularly attractive for integration into microgas-turbine systems [26], as the radial inward-flow configuration naturally accepts the air from the radial compressor at the outer periphery and delivers hot combustion products inward to the radial turbine inlet, matching both gas paths geometrically and eliminating flow-turning ducts or transition pieces that would otherwise introduce

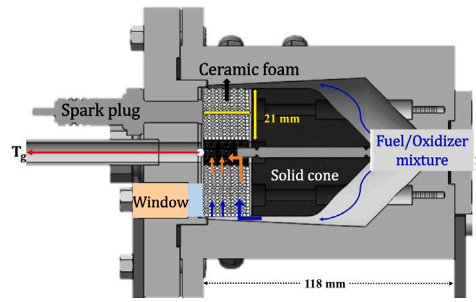

Fig. 1. Cross-sectional view of radial inflow porous media burner setup, representing fuel-air mixture direction.

additional total pressure losses. However, while the earlier work established the potential of the radial PMB concept, the influence of porous topology itself on flame stabilization, heat recirculation, and pollutant formation in this configuration has not yet been systematically resolved.

Building on these findings, the present study systematically examines how porosity gradients and gas–solid thermal coupling govern flame stabilization and pollutant formation in a radial inward-flow PMB. To this end, five SiC Voronoi-based porous structures – two uniform, two inward-graded, and one reverse-graded – are experimentally investigated using pure NH_3 and an NH_3/H_2 (70/30 vol.%) fuel blend. The analysis focuses on flame stability, solid-phase temperature distributions, and exhaust emissions in order to determine how pore architecture controls flame location, heat recirculation, combustion completeness, and the trade-off between NO, N_2O, and unburned-fuel slip. The resulting trends provide design guidance for topology-optimized porous burners targeting compact, stable, and low-emission ammonia combustion systems.

2. Experimental method

A radial inward-flow porous media burner was used to investigate NH_3–H_2–air combustion under atmospheric pressure conditions. The burner configuration, shown in Fig. 1 and described in detail in our previous study [25], was employed here to isolate the effect of porous topology. The burner consists of a cylindrical SiC porous insert into which the flow is guided via a central solid cone that redirects the reactant mixture into the porous region. The reactants enter tangentially at the outer periphery, flow radially inward through the porous matrix, and then discharge through a central exhaust passage, as depicted by the arrows in Fig. 1. An optical window integrated into the burner endwall provides optical access over approximately 2/3rds of the porous radius.

The NH_3, H_2, and air flow rates were metered by mass flow controllers (Alicat MCR-250 SLPM, Alicat MCS-50 SLPM, and Bronkhorst F201CV) under ambient conditions. Burner-wall and exhaust temperatures were monitored continuously by thermocouple to ensure repeatable steady operation. All emission measurements were recorded only after the burner reached thermal steady state, confirmed by stable thermocouple readings at the burner wall (K-type, 1/8″ diameter) and exhaust (R-type, 1/8″ diameter) for a minimum of two minutes. Exhaust-gas composition was measured downstream of the porous media. NO and residual O_2 were measured using a Testo-340 gas analyzer, with reported uncertainties of ±18% for NO and ±1% for O_2. N_2O and unburned NH_3 were quantified by Fourier-transform infrared (FTIR) spectroscopy with a combined uncertainty of ±5.8%, and H_2 is measured by gas chromatography (GC) with ±5%. The reported uncertainties account for repeatability, calibration, and instrument contributions, and the detailed information on the subject is provided in Supplementary Section 2.2. Run-to-run repeatability is assessed across

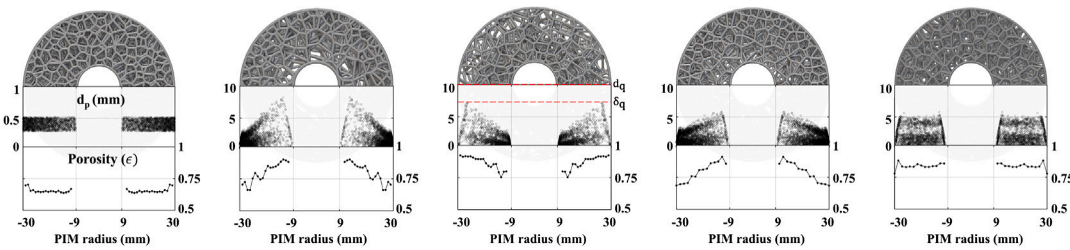

(a) PIM1 (b) PIM2 (c) PIM3 (d) PIM4 (e) PIM5

Fig. 2. Voronoi lattice structures of porous inert media 1 to 5 (left to right) with a pore diameter distribution across the thickness (d_p - top axis) and associated porosity along the radius (ϵ - bottom axis). The quenching diameter (d_q) and distance (δ_q) are included in PIM3 as scale reference markers providing physical context for the pore size ranges, corresponding to stoichiometric NH_3/air mixture at atmospheric pressure and 300 K [27,28].

independent warm-up and cool-down cycles, with a nominal deviation of 20 K in exhaust gas temperature T_g across repeated conditions.

An infrared camera (FAST M3k, Telops), operating over 1.5–5.4 μm, was used to estimate the surface temperature of the SiC porous structure during combustion. To isolate solid-phase from gas-phase emission of combustion species (NO, N_2O, NH_3, and H_2O), a narrow band-pass filter centered at 2.085 μm with a bandwidth of ±0.010 μm was employed. The filtered signal was converted to temperature using Planck's law. The SiC emissivity was taken as ϵ = 0.9 [21,29–31], which is sufficiently high for reliable radiometric temperature estimation. The uncertainty in the reported solid-surface temperature is ±5% (at 1500 K), primarily due to the temperature dependence of SiC emissivity and sapphire window transmissivity over the range encountered in the present study, the uncertainty evaluation is provided in Supplementary Section 2.1.

2.1. PIM topology

In the present radial inward-flow porous media burner, the reactant mixture enters at the outer radius and traverses the porous matrix toward the inner core, where heat released in the reaction zone recirculates upstream through solid conduction, gas–solid convection, and radiation within the porous structure, preheating the reactants and stabilizing the flame. Consequently, the local pore architecture along the radial direction governs the hydraulic resistance, gas–solid heat exchange intensity, upstream heat recirculation, and the thermal conditions under which the flame anchors and pollutants form.

The cylindrical SiC porous inserts used in this study had an outer diameter of 60 ± 1 mm, an inner diameter of 18 ± 1 mm, and a thickness of 21 ± 1 mm, with a constant strut diameter of 1.2 ± 0.4 mm. The porous inserts are manufactured by EngiCer (Switzerland) using a replica technique followed by pyrolysis and liquid silicon infiltration [32]. Visual inspection after the full experimental campaign confirmed no cracking, spallation, or structural degradation in any configuration, consistent with the well-established thermomechanical durability of similar foams under sustained high-temperature cycling (up to 1400°C, 1000 h) [33].

Five distinct porous inert media (PIM) topologies were investigated: two uniform structures (PIM1 and PIM5), two inward-graded structures (PIM2 and PIM4), and one reverse-graded structure (PIM3), as shown in Fig. 2 and summarized in Table S1 of the Supplementary Section 1. The pore diameter d_p is defined as the diameter of the largest inscribed sphere within pore cell (illustrated in Fig.S1), and together with porosity (ϵ, calculated as the void fraction), each Voronoi lattice geometry can be created using the commercial nTopology software package [34–36], more details are available in Supplementary Section 1. This architecture allows pore size and porosity to be varied independently and continuously along the radial direction facilitating seamless adaptation to extreme gradients without mathematical distortions or compromised structural interconnectedness.

PIM1 and PIM5 serve as uniform reference cases with markedly different pore scales: PIM1 is fine and relatively dense (d_p = 0.43 mm, ϵ = 0.65), whereas PIM5 is coarser and more open (d_p = 3 mm, ϵ = 0.83). PIM2 and PIM4 are inward-graded structures, in which pore diameter and porosity increase from the outer to the inner radius; however, PIM4 remains finer and less porous than PIM2. PIM3 represents the reverse-graded case, with larger pores and higher porosity at the outer radius and progressively smaller, denser cells toward the inner radius.

Although the radial velocity field contributes to local flow conditions, the velocity profiles (not shown here) present similar radial trends across all five porous inserts and indicate a broad hydrodynamic flame-trapping feature for all topologies, as thoroughly discussed in [25]. Accordingly, the principal differences among the present PIM configurations are attributed primarily to topology-dependent heat transfer and heat recirculation within the porous structure. Given the comparatively large quenching diameter of ammonia flames, pore scale is therefore expected to play a particularly important role in stabilization behavior [19,27]. Pores too small relative to quench diameter extinguish flame, while excessively large pores reduces gas–solid heat exchange and allow flame blowout under high velocity conditions.

3. Results and discussion

3.1. Flame stability

Considering that the principal differences among the present PIMs arise from topology-dependent heat recirculation and gas–solid coupling along the radial flow path, the first step is to determine how these differences modify the burner stability limits. Fig. 3 summarizes the stable operating range of the five PIM topologies as functions of reactant mass flux, $\dot{m}''$, and equivalence ratio, ϕ, for pure NH_3 and NH_3/H_2 combustion. The stability maps are constructed by varying the reactant mass flux ($\dot{m}''$, defined as the mass flow rate per unit outer surface area) over a wide range of ϕ for each PIM.

For pure ammonia ($x_{NH_3} = 1$), stable operation spans $\dot{m}''$ = 0.12–0.25 $kg\,m^{-2}\,s^{-1}$, as shown in Fig. 3(a). Over this range, the graded porous topologies exhibit substantially wider stability limits than the uniform structures. This behavior indicates that, for pure NH_3, operability is governed primarily by the interplay between the large quenching constraint of the ammonia flame and the radial increase in interstitial velocity toward the inner radius. Among the graded structures, PIM3 provides the widest stability window (0.8 ≤ ϕ ≤ 1.3). Its large outer pores (d_p = 7.0 mm) provide the greatest quenching margin in the lowest-velocity region of the burner, allowing the flame to stabilize over a broad range of equivalence ratios. However, because the pore size decreases rapidly toward the inner radius, the stable region contracts at higher $\dot{m}''$, where the inward rise in interstitial velocity increases the blowout tendency. PIM2 has a similar average pore-size range but the opposite gradient direction (refer to Table S1), so although it shows comparable operability at low mass flux, its stability limits shrink more rapidly as $\dot{m}''$ increases. PIM4 follows the

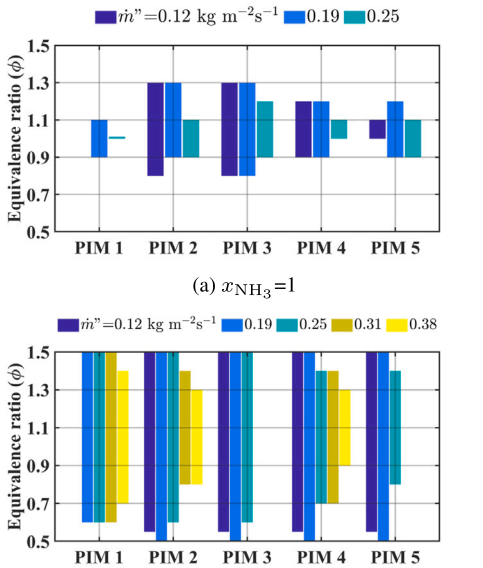

(a) x_{NH_3}=1

(b) x_{NH_3}=0.7 in NH_3/H_2 mixture ($x_{NH_3} + x_{H_2} = 1$)

Fig. 3. Stability maps across PIMs for pure NH_3 and NH_3/H_2 mixture, where, color bar denotes mass flux ($\dot{m}''$) across a range of equivalence ratios (ϕ).

same inward-graded trend as PIM2 but with finer pores throughout, leading to a still narrower stability window and indicating that the average pore scale represented by PIM2 and PIM3 is more favorable for pure NH_3 stabilization. Among the uniform structures, PIM1 – the finest and densest topology investigated (d_p = 0.43 mm and ϵ = 0.65)-– exhibits the narrowest operating range, because its pore size remains well below the characteristic quenching threshold across both lean and rich conditions [27]. PIM5, although also uniform, has substantially larger pores (d_p = 3 mm), which provide a larger quenching margin and therefore support a broader stable range than PIM1. Overall, the graded topologies outperform the uniform ones because they span a broader range of pore sizes along the radial flow path, enabling flame stabilization across both the lean and rich limits while remaining compatible with the increasing inward velocity field.

Fig. 3(b) presents the stable operating range for x_{NH_3} = 0.7. The addition of hydrogen extends flame stability to $0.5 \leq \phi \leq 1.5$ across all PIMs over $\dot{m}''$ = 0.12–0.38 $kg\,m^{-2}\,s^{-1}$. The operating window gradually narrows as $\dot{m}''$ increases, with the upper limit restricted to $\dot{m}''$ = 0.38 $kg\,m^{-2}\,s^{-1}$ by the exhaust-wall temperature limits of the present experimental setup. For PIM3 and PIM5, operability data are reported only up to $\dot{m}''$ = 0.25 $kg\,m^{-2}\,s^{-1}$, although stable operation at higher fluxes is likely also attainable. In contrast to pure ammonia, where the flame anchors within the porous matrix, the higher burning velocity of the NH_3/H_2 mixture promotes upstream stabilization at the outer surface, in the narrow gap between the outer diameter of the PIM and the burner wall (see Fig. 1). As a result, the internal pore architecture no longer controls the flame location, and the differences among PIM topologies that govern pure-NH_3 behavior largely collapse for this mixture. This behavior reflects a limitation of the present PMB geometry, which is better matched to the lower burning velocity and larger quenching diameter of pure NH_3 flames. The shift in flame location also changes the thermal role of the porous insert: instead of preheating the reactants and recirculating heat upstream, the matrix acts primarily as a post-flame heat sink, reducing the combustion temperature. Consequently, the characteristic benefits of porous-media combustion are not fully realized under x_{NH_3} = 0.7 conditions, consistent with literature [25].

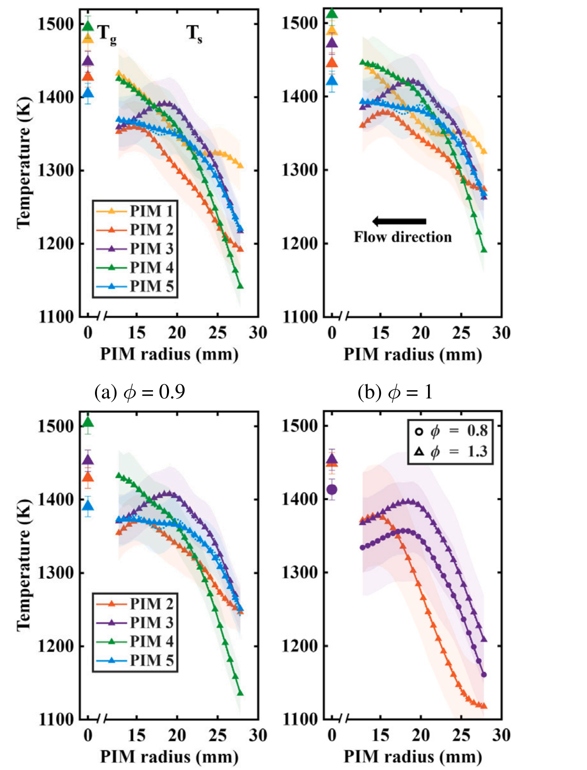

(a) ϕ = 0.9 (b) ϕ = 1 (c) ϕ = 1.2 (d) ϕ = 0.8 and 1.3

Fig. 4. Radial solid temperature profile (T_s) and associated exhaust gas temperature (T_g) for all PIMs burning x_{NH_3} = 1 at $\dot{m}''$ = 0.19 $kg\,m^{-2}\,s^{-1}$ across various ϕ.

3.2. Solid matrix temperature

The solid matrix temperature provides a direct measure of heat exchange between the gas phase and the porous structure, offering insight into the thermal behavior of each PIM topology. The measured solid matrix temperature distribution for all five PIMs during pure ammonia combustion (x_{NH_3} = 1), at a fixed mass flux of $\dot{m}''$ = 0.19 $kg\,m^{-2}\,s^{-1}$ and over a range of equivalence ratios, is presented in Fig. S3. Additionally, the average solid temperature (T_s) of the porous structure along the centerline and the exhaust gas temperature (T_g) measured immediately downstream of the inner radius are reported. For clarity, the results are displayed as smoothing splin fits (smoothing parameter 0.5), presented in line charts in Fig. 4.

The solid matrix temperature distributions reveal that the PIMs fall into two distinct stabilization regimes under pure ammonia combustion: dynamic stabilization, in which the flame location shifts progressively with equivalence ratio (PIM2 and PIM4), and fixed stabilization, in which the flame anchors at an invariant radial position regardless of ϕ (PIM1, PIM3, and PIM5), the criteria considered for distinguishing these modes is provided in Supplementary Section 3.2. The dynamic behavior of PIM2 and PIM4 arises from their inward-increasing pore size gradient, which produces a radially varying interphase heat exchange that shifts the preferred anchoring location as the equivalence ratio (and thus combustion temperature) is varied. These geometries effectively transfer heat from the burned gas region to the reactant flow, as evidenced by the steep temperature gradient and low upstream temperatures for these two topologies (see Fig. 4).

PIM3, despite also being a graded topology, does not exhibit dynamic stabilization: its large outer pores (d_p = 7 mm) result in flame anchoring at a mid-radius value, where the decreasing pore size intensifies, preventing the flame from progressing further downstream.

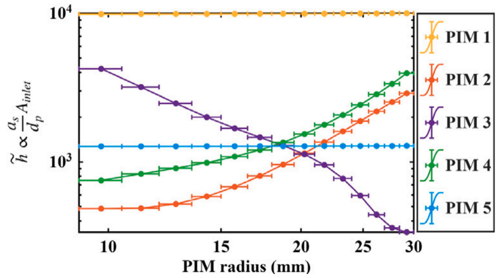

Fig. 5. Radial profile of the specific surface area (a_s, m^{-1}) to pore diameter (d_p, m) ratio non-dimesionalized by constant area of inlet annulus (A_{inlet}, m^2) for all five PIMs, representing volumetric heat transfer coefficient. Both quantities are volumetrically defined descriptors computed over a 1.5 mm radial extraction window at each position; the horizontal bars denote the spatial averaging window, not measurement uncertainty.

The fine uniform topology of PIM1 and coarse uniform topology of PIM5 stabilize at fixed locations for the expected reason: spatially constant pore structure results in a single stabilization location, and thus variation of the equivalence ratio is only possible in a narrow range under which the stabilization location is only minimally affected.

Moreover, an ordering in both flame stabilization location and peak solid temperature emerges from Fig. 4. For a fixed equivalence ratio, the flame stabilizes progressively farther downstream (more inward) along the radial gas path in the order PIM5, PIM3, PIM2, PIM4, and PIM1, best visualized in Fig.S3. The corresponding peak solid temperatures follow a different ordering, decreasing as PIM1, PIM4, PIM3, PIM5, and PIM2. The fact that these two rankings do not coincide indicates that flame location alone does not determine the thermal response of the porous media; rather, the solid-temperature field depends on both the available preheating length and the local gas–solid thermal coupling at the stabilization site.

The thermal behavior across the porous inserts can be interpreted from first principles by separating heat recirculation within the solid matrix from heat exchange between the gas and solid. In porous media burners, upstream heat recuperation is sustained primarily by solid conduction, while the rate at which this stored thermal energy is transferred to the incoming reactants is controlled by the volumetric gas–solid heat transfer coefficient. For the present burner, a first-principles estimate indicates a Biot number of order 10^{-2} (representing the ratio of internal conductive resistance within the solid phase to external convective resistance at the gas–solid interface and defined as $\mathrm{Bi} = hL_c/k_s$, where h is the interfacial heat-transfer coefficient, L_c is the characteristic solid length scale, and k_s is the solid thermal conductivity), implying that internal conduction through the solid struts remains fast compared to convective resistance, which is the limiting step for preheating and, hence, for heat recirculation effectiveness. Following the standard porous-media formulation also adopted by Vignat et al. [19,20], the volumetric gas–solid heat transfer coefficient scales as $h_v \sim a_s k_g \mathrm{Nu}/d_p$, where a_s is the specific surface area, d_p is the pore diameter, Nu is the Nusselt number, and k_g is the gas thermal conductivity. Under the present operating conditions, the interstitial velocity field is of similar magnitude across the five topologies, so that variations in Reynolds number arise primarily through the pore diameter, giving $\mathrm{Re} \sim d_p$ and therefore $\mathrm{Nu} \sim \mathrm{Re}^{0.4} \sim d_p^{0.4}$. Since the same material and gas mixture are used across all configurations, k_g remains constant. It follows that $h_v \sim a_s/d_p^{0.6}$, and the volumetric interface heat flux $q' \sim h_v(T_g - T_s)$ scales accordingly, provided the characteristic gas–solid temperature difference remains of comparable order among cases. Thus, the ratio a_s/d_p, charted in Fig. 5 (non-dimensionalized by the constant area of the inlet annulus, A_{inlet}) provides a physically meaningful surrogate for ranking the relative local heat-transfer propensity of the different PIM configurations, as it preserves the same monotonic dependence on increasing surface area (a_s) and decreasing pore size (d_p). The solid radiation is approximately two orders of magnitude higher in thermal resistance than convection at the flame stabilization location, and therefore acts primarily on the upstream heat recirculation region. The radiative heat loss fraction under these conditions is estimated to be approximately 10%, as detailed in our previous study [25].

The topology-dependent behavior in Fig. 4 is most consistently interpreted through a two-level mechanism in which the flame stabilization location is governed primarily by local pore-size compatibility with the large quenching diameter of NH_3 flames, whereas the solid-temperature response is governed by the local strength of gas–solid thermal coupling. In this sense, the a_s/d_p profiles in Fig. 5 should not be interpreted as directly shifting the flame upstream or downstream by themselves; rather, they indicate how strongly the gas is thermally coupled to the solid once a locally admissible stabilization region exists.

PIM1, with the finest pores throughout and the highest nearly uniform a_s/d_p, provides the smallest quenching margin and therefore requires the longest cumulative preheating path before a stable flame can be sustained, leading to the deepest stabilization location, beyond the optical window (<13 mm), and the highest peak solid temperature of approximately 1430 K. PIM3 represents the opposite limit: its coarse outer region provides the largest quenching margin, but its low outer-region a_s/d_p also implies weak gas–solid interaction there, so this upstream zone does not act as a strong internal anchoring region. Stable anchoring emerges only farther inward, near 20 mm, where the reverse gradient contracts the pore structure and increases both confinement and thermal coupling. Because the flame then stabilizes over a comparatively narrow radial zone, the resulting heat release is more localized, which explains why PIM3 still reaches a relatively high peak T_s of approximately 1390 K despite its more upstream stabilization location. PIM2 and PIM4 both exhibit inward-increasing pore size and porosity, so the quenching margin improves progressively along the radial direction, which explains their dynamic stabilization behavior. Between these two, PIM4 is finer overall and therefore shifts the admissible stabilization region farther inward than PIM2, while its consistently higher a_s/d_p level also yields stronger gas–solid coupling and a peak T_s about 70 K higher. PIM2, by contrast, stabilizes near 16 mm in a coarser and more weakly coupled region, and therefore exhibits the lowest peak T_s of approximately 1350 K. PIM5 remains intermediate in both pore size and thermal coupling, and correspondingly stabilizes outermost with a peak temperature between those of PIM2 and PIM3. Thus, in pure NH_3 combustion, the flame location is controlled mainly by pore-scale quenching margin and the available preheating length, whereas the a_s/d_p distribution governs the intensity of thermal coupling and the resulting solid-temperature field.

4. Pollutant emissions

Pollutant formation differs fundamentally between pure NH_3 and NH_3/H_2 operation because the flame stabilization location changes with fuel blend. Under pure NH_3, the flame anchors inside the porous matrix, whereas under H_2 enrichment it shifts to the outer surface, changing the governing thermal mechanism and the resulting emissions hierarchy.

Under pure NH_3 combustion, the dominant NO formation route is fuel-bound nitrogen oxidation, because the flame temperatures are generally insufficient to activate the thermal Zeldovich mechanism [37]. As shown in Fig. 6(a), NO therefore follows the expected equivalence-ratio dependence, with all four PIMs reaching their highest values near stoichiometric conditions and remaining at or below 2000 ppm (normalized to 15% O_2). Under richer conditions ($\phi \geq 1.2$), NO decreases substantially as reduced O_2 availability and increased NH_2 concentration shift the chemistry away from NO production and toward N_2 formation [38]. PIM1 is excluded from Fig. 6 because its operating range at $\dot{m}'' = 0.19\ \mathrm{kg\,m^{-2}\,s^{-1}}$ is too narrow for meaningful comparison,

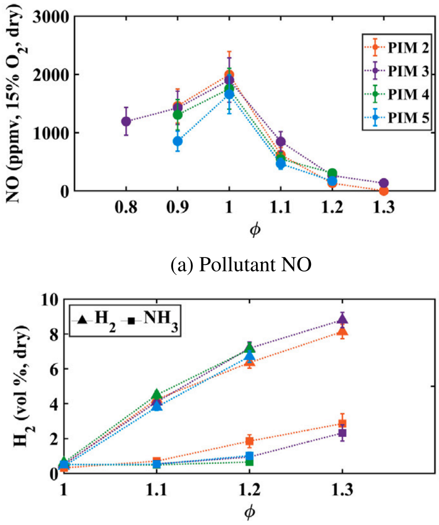

(a) Pollutant NO

(b) Unburned NH_3 and H_2 slip

Fig. 6. Emissions for pure NH_3 combustion at $\dot{m}'' = 0.19$ kg m^{-2} s^{-1} across PIM topologies (PIM2 to PIM5), (a) NO, and (b) Unburned NH_3 and H_2 slip.

and the PIM2 data are reproduced from our previous study for direct comparison [25]. Among the remaining configurations, PIM5 records the lowest NO, consistent with its lowest exhaust-gas temperature, T_g, in Fig. 4. This is further supported by its N_2O emission of 170 ppmv at $\phi = 0.9$, the highest among the four PIMs at that condition and the only value above the 100 ppm detection threshold, indicating operation in a regime where N_2O survives rather than decomposes [37]. By contrast, PIM2, PIM3, and PIM4 show similar NO levels within experimental uncertainty across ϕ, although the lower peak T_s previously observed in PIM2 is consistent with less complete combustion near stoichiometric operation [25].

Under rich conditions, unburned NH_3 and H_2 slip become the clearest indicators of combustion completeness, because the lower O/H ratio shifts ammonia oxidation toward nitrogen hydride intermediates and suppresses oxide formation [38]. Accordingly, both NH_3 and H_2 slip increase monotonically with increasing ϕ, with H_2 remaining the dominant unburned product. At $\phi = 1.0$–1.1, the differences among PIMs are relatively small. By $\phi = 1.2$, however, the slip trends clearly reflect the thermal hierarchy established in Fig. 4(c). PIM2, which exhibits the lowest peak T_s, yields the highest NH_3 slip (0.37 vol%, normalized to 15% O_2) and the lowest H_2 concentration (6.35 vol%), indicating poor ammonia conversion in the coarser and more weakly coupled region where the flame anchors. PIM5 performs somewhat better than PIM2 because its moderate and spatially uniform topology provides more consistent preheating, although both still exhibit NH_3 levels that would require post-treatment. PIM3 shows intermediate behavior, consistent with flame stabilization near mid-radius and partial heat recirculation from the inner portion of the insert. PIM4 exhibits the highest peak T_s and correspondingly the strongest preheating, producing the lowest NH_3 slip (0.13 vol%) and the highest H_2 concentration (7.12 vol%). Under pure NH_3 operation, the emissions hierarchy therefore follows the combustion completeness set by the internal flame location and the associated thermal environment.

Fig. 7 presents the measured NO, N_2O, and unburned NH_3 and H_2 emissions for PIM3, PIM4, and PIM5 under H_2-enriched operation ($x_{NH_3} = 0.7$) at $\dot{m}'' = 0.19$ kg m^{-2} s^{-1}. As established in the flame-stability analysis, hydrogen enrichment fundamentally alters the governing mechanism because the higher laminar burning velocity shifts the flame from the interior of the porous matrix to the outer surface of the media [25]. Emissions are therefore no longer controlled by internal heat recirculation, but primarily by the thermal environment at

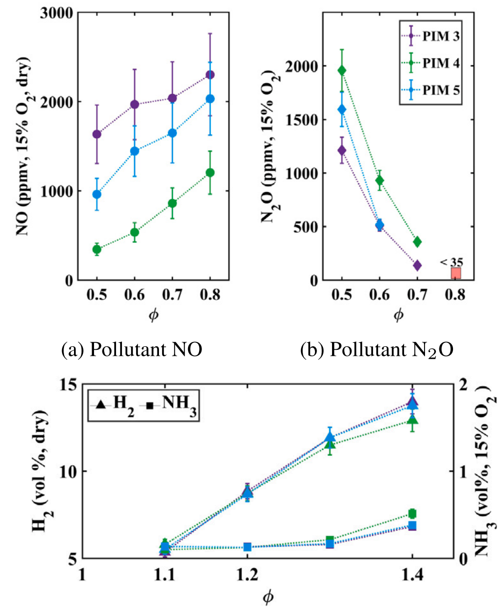

(a) Pollutant NO

(b) Pollutant N_2O

(c) Unburned NH_3 and H_2 slip

Fig. 7. Emissions for NH_3/H_2 combustion at $\dot{m}'' = 0.19$ kg m^{-2} s^{-1} across PIM topologies (PIM3 to PIM5), (a) NO, (b) N_2O, and (c) Unburned NH_3 and H_2 slip.

the outer flame, which is set by the outer-region topology. Among the three configurations, the outer-region a_s/d_p follows the order PIM4 > PIM5 > PIM3 (Fig. 5), implying progressively stronger heat extraction from the flame in the same order.

For lean operation, NO decreases with decreasing ϕ across all three PIMs, consistent with the reduction in heat release rate and flame temperature as lean extinction is approached. Over the same range, N_2O increases sharply at very lean conditions ($\phi \leq 0.6$), where lower flame temperatures favor N_2O survival and suppress its thermal decomposition [37]. The resulting NO/N_2O trade-off is particularly clear at $\phi = 0.5$: NO follows PIM3 (1635 ppm) > PIM5 (962 ppm) > PIM4 (344 ppm), while N_2O follows the reverse order, PIM4 (1957 ppm) > PIM5 (1593 ppm) > PIM3 (1212 ppm). This ordering is consistent with the outer-region topology. PIM3, which has the lowest outer-region a_s/d_p, extracts the least heat from the outer-surface flame and therefore supports the hottest flame among the three configurations, favoring NO formation while also allowing more complete N_2O decomposition. PIM4 lies at the opposite extreme: its high outer-region a_s/d_p extracts heat most strongly, suppressing flame temperature, minimizing NO, and maximizing N_2O. PIM5 remains intermediate in both thermal behavior and emissions. Near lean extinction, this stronger outer-surface cooling also contributes to incomplete combustion, as reflected by the NH_3 slip of 1.76 vol% in PIM4 and 0.89 vol% in PIM5 at $\phi = 0.5$.

The rich-side emissions under $x_{NH_3} = 0.7$ are consistent with the same ordering. Unburned NH_3 and H_2 slip increases as ϕ increases, and the ranking among PIMs follows the thermal environment imposed by the outer-region topology. In particular, PIM3, which extracts the least heat from the flame, exhibits the highest H_2 slip, reaching 14 vol% at $\phi = 1.4$. Thus, for H_2-enriched operation, the topology dependence is governed mainly by heat loss at the outer-surface flame rather than by internal flame stabilization or internal heat recirculation.

The same mechanism persists at the lower mass flux of $\dot{m}'' = 0.12$ kg m^{-2} s^{-1}, where the burner operates near the lean-extinction limit. Our previous study showed that PIM2 produces reduced NO at these conditions because the lower combustion temperature suppresses fuel-N oxidation [25]. Fig. 8 extends this comparison to PIM3 and PIM4

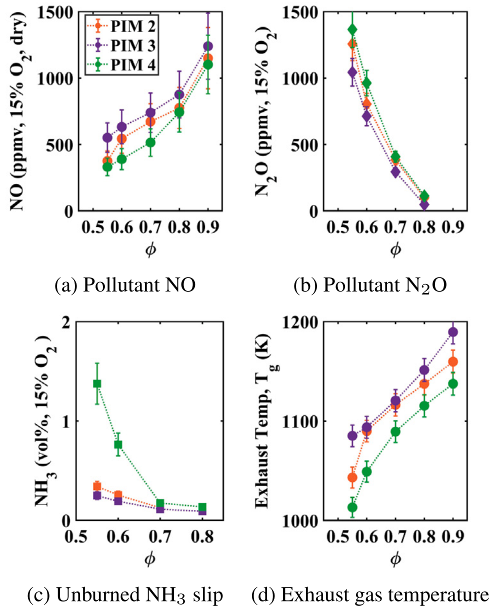

Fig. 8. Emissions for blended fuel $x_{NH_3} = 0.7$ under lean combustion at mass flux of $\dot{m}'' = 0.12$ kg m^{-2} s^{-1} across PIM topologies (PIM2 - 4), (a) NO, (b) N_2O, (c) NH_3 slip, (d) Exhaust gas temperature T_g.

over $0.55 \leq \phi \leq 0.9$. Even in this lower-temperature regime, the outer-region topology remains the dominant discriminator, with PIM3 and PIM4 again bracketing the a_s/d_p range among the tested inserts. The same opposing NO and N_2O trends persist, now reinforced by the lower measured exhaust-gas temperatures in Fig. 8(d). Despite the outer-surface flame stabilization, the radial PMB still exhibits substantially lower NO than the single-stage axial PMB reported by Vignat et al. [19] over the lean regime $0.55 \leq \phi \leq 0.7$. Specifically, NO ranges from 551 to 740 ppmv in PIM3, which is the highest of the three configurations, while PIM4 reduces NO further to 331–552 ppmv. This reduction, however, comes at the cost of substantially higher N_2O emissions, ranging from 409 to 1366 ppm in PIM4. The corresponding NH_3 slip also becomes significant near lean extinction, reaching 1.37 vol% in PIM4, although it decreases rapidly with increasing ϕ.

Within the radial PMB configurations, the outer-region topology therefore sets the magnitude of the NO/N_2O trade-off. At $\phi = 0.7$, PIM2 reduces NO by approximately 10% relative to PIM3 while increasing N_2O by about 30%; PIM4 reduces NO by a further 24% relative to PIM2 while increasing N_2O by 6%. These results establish the NO/N_2O trade-off as the central design constraint for radial inward-flow PMBs operating on NH_3/H_2 blends. No single topology simultaneously minimizes all emissions, and the optimum design therefore depends on the relative importance assigned to local air-quality impact (NO) and greenhouse-gas impact (N_2O, 265× CO_2-equivalent over a 100-year horizon).

Conclusions

This study examined how porous topology influences flame stabilization, thermal behavior, and emissions in a radial inward-flow porous media burner for ammonia combustion. By comparing five SiC Voronoi porous inserts – two uniform, two inward-graded, and one reverse-graded – the results establish how pore scale, porosity level, and gradient direction govern operability and combustion behavior in compact radial PMBs.

For pure NH_3 combustion, the results show that flame stabilization is governed primarily by pore-scale quenching margin together with the available preheating length along the radial flow path. The graded topologies extended the stable operating range relative to the uniform structures, whereas the fine uniform insert produced the narrowest stability limits due to its small pore size and strong quenching constraint. Two distinct stabilization regimes were identified: dynamic stabilization in the inward-graded configurations, in which the flame location shifts with equivalence ratio, and fixed stabilization in the uniform and reverse-graded structures. The solid-temperature measurements further showed that the thermal response of the porous insert is governed by gas–solid coupling, with the peak solid temperature reflecting the combined effects of flame location and local heat-transfer propensity. Under rich pure-NH_3 conditions, combustion completeness followed this thermal hierarchy, with stronger preheating leading to lower NH_3 slip and higher H_2 production.

Under NH_3/H_2 operation, the governing mechanism changes fundamentally because hydrogen enrichment shifts the flame from the interior of the porous matrix to its outer surface. In this regime, the porous insert no longer acts primarily as an internal heat-recirculating medium, but rather as a heat sink that modifies the local flame temperature through the outer-region topology. As a result, the emissions behavior becomes dominated by a NO/N_2O trade-off: stronger outer-region heat extraction suppresses NO but promotes N_2O and, near lean extinction, increases NH_3 slip. Compared with conventional axial PMBs, the radial configuration nevertheless maintains lower NO emissions in the lean regime. Overall, these findings show that porous topology is a primary design variable in radial ammonia PMBs, governing not only flame stabilization and combustion completeness, but also the trade-off between low-emission performance and stable operation.

Declaration of competing interest

The authors declare that they have no known competing financial interests or personal relationships that could have appeared to influence the work reported in this paper.

Acknowledgments

This work was supported by the Israeli Innovation Authority, contract number 88853. The authors also acknowledge the financial support by the Minerva Research Center, Max Planck society contract No. AZ5746940764. The authors would also like to thank Avital Yamin, Alex Kleiman, Yohai Abraham, and David Peles, for their technical assistance.

Appendix A. Supplementary data

Supplementary material related to this article can be found online at https://doi.org/10.1016/j.proci.2026.106281.

References

[1] J. Howell, M. Hall, J.L. Ellzey, Combustion of hydrocarbon fuels within porous inert media, Prog. Energy Combust. Sci. 22 (2) (1996) 121–145.

[2] D. Trimis, F. Durst, Combustion in a porous medium-advances and applications, Combust. Sci. Technol. 121 (1–6) (1996) 153–168.

[3] M.A. Mujeebu, M.Z. Abdullah, M.A. Bakar, A. Mohamad, R. Muhad, M. Abdullah, Combustion in porous media and its applications–A comprehensive survey, J. Environ. Manag. 90 (8) (2009) 2287–2312.

[4] D. Mohaddes, C.T. Chang, M. Ihme, Thermodynamic cycle analysis of superadiabatic matrix-stabilized combustion for gas turbine engines, Energy 207 (2020) 118171.

[5] S. Chalia, M. Naagar, P. Thakur, A. Thakur, S. Sridhara, An overview of ceramic materials and their composites in porous media burner applications, Ceram. Int. 47 (8) (2021) 10426–10441.

[6] S. Sobhani, D. Mohaddes, E. Boigne, P. Muhunthan, M. Ihme, Modulation of heat transfer for extended flame stabilization in porous media burners via topology gradation, Proc. Combust. Inst. 37 (4) (2019) 5697–5704.

[7] S. Sobhani, P. Muhunthan, E. Boigné, D. Mohaddes, M. Ihme, Experimental feasibility of tailored porous media burners enabled via additive manufacturing, Proc. Combust. Inst. 38 (4) (2021) 6713–6722.

[8] Y. Zhang, P. Qiu, X. Li, W. Zhang, Y. Zhao, S. Sun, L. Zhang, R. Liu, Experimental and numerical study of CH4/air porous media combustion with topology gradation at elevated pressure, Appl. Therm. Eng. (2025) 129522.
[9] X. Li, R. Liu, Y. Zhang, J. Zhu, M. He, Y. Zhao, P. Qiu, L. Zhang, Effect of graded structure on CH4/air combustion in porous media burner, Fuel 407 (2026) 137570.
[10] E. Flores-Montoya, P.-A. Masset, T. Schuller, L. Selle, Flame-front tracking in porous media burners, Combust. Flame 267 (2024) 113597.
[11] A. Saha, N. DiReda, S. Sobhani, Enhancing flame stability in porous media burners via topological tuning, Proc. Combust. Inst. 40 (1–4) (2024) 105703.
[12] N. DiReda, G. D'Orazio, S. Sobhani, Thermal and structural performance of additively manufactured ceramic porous media burners, J. Eur. Ceram. Soc. 44 (4) (2024) 2271–2279.
[13] J. Li, S. Lai, D. Chen, R. Wu, N. Kobayashi, L. Deng, H. Huang, A review on combustion characteristics of ammonia as a carbon-free fuel, Front. Energy Res. 9 (2021) 760356.
[14] W.S. Chai, Y. Bao, P. Jin, G. Tang, L. Zhou, A review on ammonia, ammonia-hydrogen and ammonia-methane fuels, Renew. Sustain. Energy Rev. 147 (2021) 111254.
[15] A.A. Khateeb, T.F. Guiberti, X. Zhu, M. Younes, A. Jamal, W.L. Roberts, Stability limits and NO emissions of technically-premixed ammonia-hydrogen-nitrogen-air swirl flames, Int. J. Hydrog. Energy 45 (41) (2020) 22008–22018.
[16] X. Zhu, A.A. Khateeb, T.F. Guiberti, W.L. Roberts, NO and OH* emission characteristics of very-lean to stoichiometric ammonia–hydrogen–air swirl flames, Proc. Combust. Inst. 38 (4) (2021) 5155–5162.
[17] I.A. Makaryan, I.V. Sedov, C. Munoz-Herrera, M. Toledo, E.A. Salgansky, Combustion of ammonia-blended fuels in porous media burners, with storage and distribution implications: A review, Renew. Sustain. Energy Rev. 220 (2025) 115884.
[18] G. Vignat, B. Akoush, E.R. Toro, E. Boigné, M. Ihme, Combustion of lean ammonia-hydrogen fuel blends in a porous media burner, Proc. Combust. Inst. (2022).
[19] G. Vignat, T. Zirwes, E.R. Toro, K. Younes, E. Boigné, P. Muhunthan, L. Simitz, D. Trimis, M. Ihme, Experimental and numerical investigation of flame stabilization and pollutant formation in matrix stabilized ammonia-hydrogen combustion, Combust. Flame 250 (2023) 112642.
[20] G. Vignat, T. Zirwes, É. Boigné, M. Ihme, Experimental demonstration of a two-stage porous media burner for low-emission ammonia combustion, Proc. Combust. Inst. 40 (1–4) (2024) 105491.
[21] T. Zirwes, G. Vignat, E.R. Toro, E. Boigné, K. Younes, D. Trimis, M. Ihme, Improving volume-averaged simulations of matrix-stabilized combustion through direct X-ray μCT characterization: Application to NH3/H2-air combustion, Combust. Flame 257 (2023) 113020.
[22] S. Wei, F. Su, W. Zhou, C. Li, K. Zhang, L. Hu, Numerical simulation study on the influence of the specific surface area of honeycomb on the NH3/H2/air premixed combustion process, Int. J. Hydrog. Energy 199 (2026) 152908.
[23] H. Zhang, J. Zhou, J. Du, Z. Yu, X. Liang, Y.-B. Cheng, Y. Wang, Ammonia-methane flames stabilized in an ordered porous media burner, Energy Fuels 39 (13) (2025) 6654–6670.
[24] H. Zhang, B. Cui, J. Du, Z. Yu, X. Liang, Y.-B. Cheng, Y. Wang, Combining staged combustion and oxygen enrichment for stable and low-NOx porous media combustion of ammonia, Fuel 410 (2026) 137894.
[25] G.M. Nayak, B. Cukurel, J.K. Lefkowitz, A study on combustion characteristics of radial inward flow porous media burners for ammonia-hydrogen flames, in: Turbo Expo, Vol. 88780, American Society of Mechanical Engineers, 2025, V03AT04A043.
[26] L. Badum, B. Leizeronok, B. Cukurel, New insights from conceptual design of an additive manufactured 300 w microgas turbine toward unmanned aerial vehicle applications, J. Eng. Gas Turbines Power 143 (2) (2021) 021006.
[27] X. Yao, H. Wang, W. Zhou, J. Gao, Experimental and kinetic modeling studies of quenching diameters of laminar premixed flames of NH3/air mixtures, Combust. Flame 279 (2025) 114312.
[28] J.K. Moses, T.A. Tivfa, N.A. Qasem, A.B. Alquaity, Combustion characteristics of hydrogen, ammonia, and their blends: A review, Fuel 388 (2025) 134404.
[29] G. Neuer, G. Jaroma-Weiland, Spectral and total emissivity of high-temperature materials, Int. J. Thermophys. 19 (3) (1998) 917–929.
[30] V. Zolotarev, High-temperature spectral emissivity of SiC in the IR range, Opt. Spectrosc. 103 (2007) 592–602.
[31] S. Hatzl, M. Kirschner, V. Lippig, T. Sander, C. Mundt, M. Pfitzner, Direct measurements of infrared normal spectral emissivity of solid materials for high-temperature applications, Int. J. Thermophys. 34 (2013) 2089–2101.
[32] S. Gianella, D. Gaia, A. Ortona, High temperature applications of Si-SiC cellular ceramics, Adv. Eng. Mater. 14 (12) (2012) 1074–1081.
[33] G. D'Amico, Si-SiC based materials obtained by infiltration of silicon: study and applications, 2015.
[34] nTop Inc., nTop, New York, NY, 2024.
[35] M. Pelanconi, E. Rezaei, A. Ortona, Cellular ceramic architectures produced by hybrid additive manufacturing: A review on the evolution of their design, J. Ceram. Soc. Japan 128 (9) (2020) 595–604.
[36] H.-Y. Lei, J.-R. Li, Z.-J. Xu, Q.-H. Wang, Parametric design of voronoi-based lattice porous structures, Mater. Des. 191 (2020) 108607.
[37] S. Quan, J. Mei, D. Li, Y. Huang, Z. Li, X. Zhu, H. Wang, X. Yang, M. Zhang, R.-G. Kim, A comprehensive evaluation of kinetic reaction mechanisms for NO and N2O emissions during NH3/H2 combustion across multi-temperature regimes, J. the Energy Inst. (2025) 102260.
[38] H. Kobayashi, A. Hayakawa, K.K.A. Somarathne, E.C. Okafor, Science and technology of ammonia combustion, Proc. Combust. Inst. 37 (1) (2019) 109–133.